J Seismol (2012) 16:657–668
DOI 10.1007/s10950-012-9296-5

ORIGINAL ARTICLE

Strain rotation coupling and its implications on the measurement of rotational ground motions

Martin van Driel · Joachim Wassermann · Maria Fernanda Nader · Bernhard S. A. Schuberth · Heiner Igel

Received: 27 October 2011 / Accepted: 7 March 2012 / Published online: 28 March 2012

Abstract Spatial derivatives of the seismic wave field are known to be sensitive to various site effects (e.g., cavity effects, topography, and geological inhomogeneities). In this study, the focus is on strain rotation coupling that can cause significant differences between point measurements compared to array-derived rotational motions. The strain rotation coupling constants are estimated based on finite element simulations for inhomogeneous media as well as for the 3D topography around Wettzell, Germany (the location of the G ring laser). Using collocated array and ring laser data, the coupling constants of the ring laser itself are shown to be small. Several examples are shown to illustrate the order of magnitude that strain-induced rotation might have on the seismograms in the near field of volcanoes as well as in the far field and in the low-frequency spectrum (free oscillations).

Keywords Rotational seismology · Strain rotation coupling · Strain-induced rotation · Site effects

M. van Driel · J. Wassermann · M. F. Nader · H. Igel
Department of Earth and Environmental Sciences,
Ludwig-Maximilians-University,
Munich, Germany

B. S. A. Schuberth
Université de Nice Sophia-Antipolis,
Centre National de la Recherche Scientifique
(UMR 6526), Observatoire de la Côte d'Azur,
Géoazur, Les Lucioles 1, Sophia Antipolis,
250 Rue Albert Einstein, 06560
Valbonne, France

Present Address:
M. van Driel (✉)
Institute of Geophysics, ETH Zurich,
Zurich, Switzerland
e-mail: vandriel@erdw.ethz.ch

1 Introduction

Measuring the rotational component of the seismic wave field is more challenging than it may appear at first glance: To this day, there is no sensor commercially available that suits the needs of the different branches in seismology, i.e., strong and weak motion seismology. Although this might change in the near future, studies carried out so far either used prototypes or large observatory installations (e.g., Schreiber et al. 2009, 2006, 2003; Nigbor 1994; Graizer 2009; Dunn et al. 2009; Igel et al. 2007; Suryanto et al. 2006), sensors with questionable reliability as the Eentec R1/R2 (e.g., Bernauer et al. 2012; Nigbor et al. 2009; Wassermann et al. 2009; Evans et al. 2010), or seismic array methods (e.g., Langston 2007a, b, c; Spudich et al. 1995; Spudich and Fletcher 2009; Suryanto et al. 2006). This study will show that

array-derived rotational observations might have intrinsic differences to direct point measurements.

1.1 Point measurements

Several physical principals have been used to directly measure rotations, among which are multipendulums (e.g., Graizer 2009), liquid filled tori (e.g., Nigbor et al. 2009), and optical gyros (e.g., Schreiber et al. 2009). Rigidly attaching a three-component rotational sensor to a three-component seismometer would allow for measuring all six degrees of freedom of this rigid body and thus for recovering its complete trajectory (Lin et al. 2010). In seismology, it is normally valid to assume the rotation angles to be "small" and neglect second-order terms. Therefore, the dominant effect of rotations on translational seismograms is the changing projection of gravity onto the horizontal seismometer components due to tilt (Graizer 2010). Correcting seismograms for this tilt effect can be done if the effective tilt of the seismometer is measured with appropriate accuracy.

1.2 Array measurements

Another approach to measure rotational motions are seismic arrays: Sampling the wave field in adjacent locations, it is possible to estimate the full spatial gradient of the wave field (at the free surface, see Spudich et al. 1995; Spudich and Fletcher 2009; Suryanto et al. 2006), i.e., rotation as well as normal and shear strain. The method is based on the assumption that the deformation is linear over the array area. Local site effects at single stations are neglected and averaged out if enough stations are used. Due to these site effects and in contrast to point measurements, arrays do not necessarily measure the rotation of the single stations and can thus not be used for tilt correction.

Spudich et al. (1995) and Spudich and Fletcher (2008, 2009) present a method to solve the involved linear problem including a thorough error analysis. Their Matlab code has been translated to the Python scripting language (www.python.org) and included in the ObsPy toolbox (Beyreuther et al. 2010; Megies et al. 2011).

2 Site effects in the measurement of spatial derivatives of the displacement field

Several studies have shown that the spatial derivatives of the displacement field are strongly affected by site effects, i.e., cavity and topography effects as well as geological inhomogeneities (e.g., Harrison 1976; Gomberg and Agnew 1996; Berger and Beaumont 1976; Kohl and Levine 1995). In strong-motion seismology, the observed rotational motions often exceed those expected for homogeneous linear estimates by a factor of 10 or even more. This is likely to be caused by strong near surface heterogeneities and the strong-motion siting standards (John R. Evans, pers. comm.). For the rotational component of the wave field (i.e., the antisymmetric part of the gradient), one important site effect is strain rotation coupling (SRC), also called strain-induced rotation.

2.1 Strain rotation coupling

Strain rotation coupling is a locally acting site effect, which converts strain on a large scale (wavelength of the seismic wave field) to rotation on a local scale. Assuming linear elasticity for the subsurface structure and for small deformations (in the sense that the small angle approximation is valid), this effect is also linear and the coupling constants can be defined as (Harrison 1976; Wielandt and Forbriger 1999):

$$c_{ij} = \frac{\omega_j}{\epsilon_i} = \frac{\text{strain-induced rotation around } j\text{-axis}}{\text{strain component } i} \quad (1)$$

Both strain and rotation are dimensionless and therefore the coupling constants as well.

Following Cochard et al. (2006, Eq. (7)), at the free surface, the normal strain perpendicular to the surface is a linear combination of the normal stresses parallel to it. Additionally, shear stress in planes perpendicular to the surface is zero, so the strain tensor has three degrees of freedom only: the two horizontal normal strains and horizontal shear strain (which will be denoted in the coupling constants with index $_S$).

Few authors have tried to estimate coupling constants so far, among which are Harrison

(1976), who found values of up to 1.5 for the coupling constants in 2D simulations on large structures (east–west section of the Rocky Mountains). Lambotte et al. (2006) used earth tide simulations and data to determine coupling constants for GNI, MAJO, and BFO stations and found maximum values up to 0.8 at BFO for normal strain and 1.4 for shear strain. Wielandt and Forbriger (1999) estimated coupling constants of up to 0.3, comparing tilts estimated with a relation between horizontal and vertical seismograms by assuming a volumetric point source (Mogi 1958) to finite differences of the vertical components of two seismometers at Stromboli volcano (Italy). Comparing the results of two field experiments, they conclude that most of the local (point measured) tilt was controlled by the instrument installation procedure.

2.2 Simulating coupling constants for inhomogeneous media

In this section, the aim is to quantify the strain rotation coupling effect of inhomogeneities on the scale of the size of the seismometer foundation that are often found for example at seismic stations installed in volcanic environments. In the seismic wave equation for linear elastic inhomogeneous media (e.g., Nolet 2008, Eq. 2.42), the time-dependent term can be neglected, assuming that the domain of interest (the site of the seismometer) is small compared to the seismic wavelength: The boundary conditions then change orders of magnitude slower than the model adapts to them. The instantaneous differential equation governing the deformation of the site, using the strain of the wave field as boundary condition, then reads:

$$\nabla\cdot\left[\mu\left(\nabla\mathbf{u}+(\nabla\mathbf{u})^T\right)\right]+\nabla\left(\lambda\nabla\cdot\mathbf{u}\right)=\rho\frac{\partial^2\mathbf{u}}{\partial t^2}\approx 0 \qquad (2)$$

Here λ and μ denote the Lamè parameters, ρ the density, the superscript T is the transpose, and ∇ the Del operator.

Using the escript/finley PDE solver module for Python (Gross et al. 2007a, b), this equation can be solved numerically using the preconditioned conjugate gradient method. The model (see Fig. 1) consists of a cuboid two-phase medium, generated by clipping a Gaussian random medium: First, a 3D array of normally distributed random numbers is generated and low-pass-filtered at the desired correlation length (e.g., Yoon 2005). Next, the absolute value is clipped at 20% of the maximum amplitude and interpolated to the mesh.

The baseplate of the seismometer has a bulk modulus of $\lambda = 50$ GPa and an artificially high shear modulus of $\mu = 1{,}000$ GPa to prevent it from bending. This causes the rotation to be constant over the baseplate. The size of the domain was chosen empirically to be larger than 8 and smaller than 20 correlation lengths of the Gaussian medium; the mesh consists of 166,400 hexahedrons. Tests with 25% larger domain and 25% higher mesh resolution showed no significant influence on the results.

In post-processing, the rotation is computed as antisymmetric part of the gradient and averaged over the baseplate. Using the definition (Eq. 1), an estimate of the coupling constants c_{xx}, c_{xy}, and c_{xz} is obtained. Doing so for many randomly

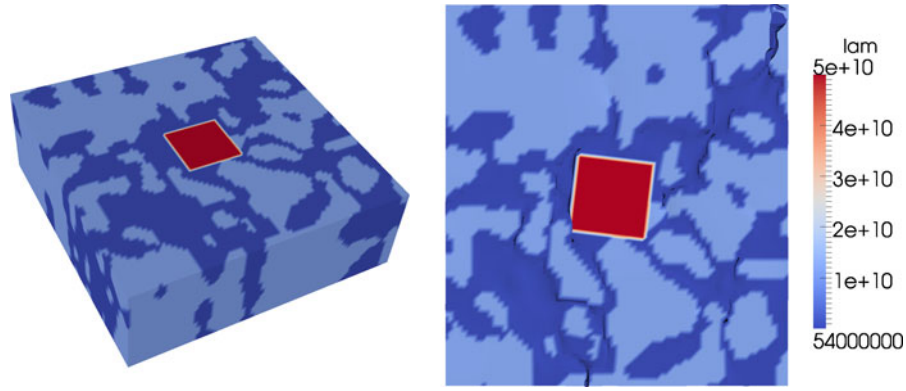

Fig. 1 Sample 3D random model ($3 \times 3 \times 1$ m^3), *right*: imposed normal strain $\epsilon_{xx} = 10^{-6}$, deformation exaggerated by a factor of 10^5, local rotations caused by inhomogeneities

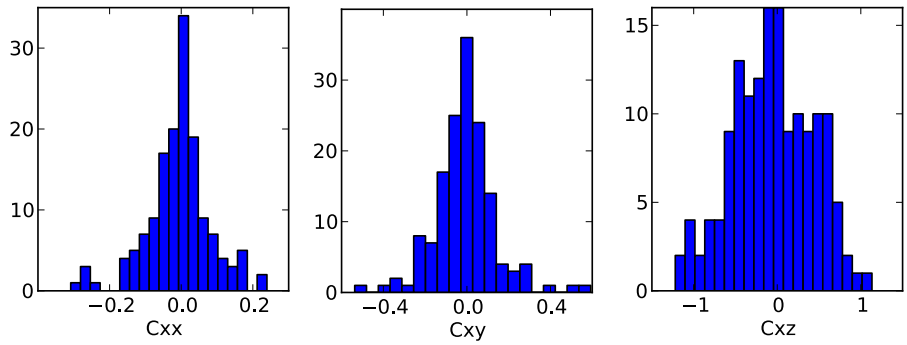

Fig. 2 Histograms of coupling constants for 150 random models as in Fig. 1, strain in x-direction and rotation around x, y, and z, respectively, standard deviations are 0.09, 0.15, and 0.48

generated ground models, a symmetrical distribution with zero mean is obtained (see Fig. 2). The width (standard deviation) is thus characteristic for the coupling that can be expected for the input parameter set.

2.3 Statistical analysis

To investigate the parameter space more systematically, it is necessary to reduce the number of parameters—not only to reduce computational cost but also to get a more general solution. In addition, it is impossible to simulate the coupling constants for a specific site because of the limited knowledge of the local subsurface structure. The aim of this study is an order of magnitude estimation for the width of the distributions rather than exact numbers for specific models.

The model presented above needs a few essential parameters: the Lamé constants of the medium ($\lambda_1, \lambda_2, \mu_1, \mu_2$), the correlation length (a), and the (quadratic) plate size (l). All other parameters (model size, mesh spacing, etc.) are chosen such that they do not influence the results in first order.

The first strict assumption is $\lambda = \mu$. It is obvious that multiplying μ (and hence λ) by a constant factor does not change the solution $\mathbf{u}$ of Eq. 2, if the boundary conditions are formulated as imposed strain (Dirichlet). This motivates the definition of the dimensionless contrast $\delta := \frac{\mu_1 - \mu_2}{\mu_1}$. Scaling the whole model, keeping the ratio of correlation length a and plate size l and additionally the strain constant, all angles and hence the coupling constants remain the same. The two lengths can therefore be replaced by the length parameter $\frac{a}{l}$.

The results of this parameter study are presented in Fig. 3 for the normal strain in the x-axis: Each pixel represents at least 40 randomly distributed models with a symmetric distribution of coupling constants as in Fig. 2. The color scale shows the standard error as a measure of the width of these distributions as a function of dimensionless contrast and the length parameter. The statistic error of the standard error as an estimation for the standard deviation is $1/\sqrt{2N} \approx 12\%$, which is acceptable as we are only interested in the order of magnitude.

The standard deviations for normal strain in y and for shear strain can be derived from the results for strain in x without the need for further simulations: Normal strain in y causes the same distributions as in x for symmetry reasons. Shear strain can be written as the sum of perpendicular

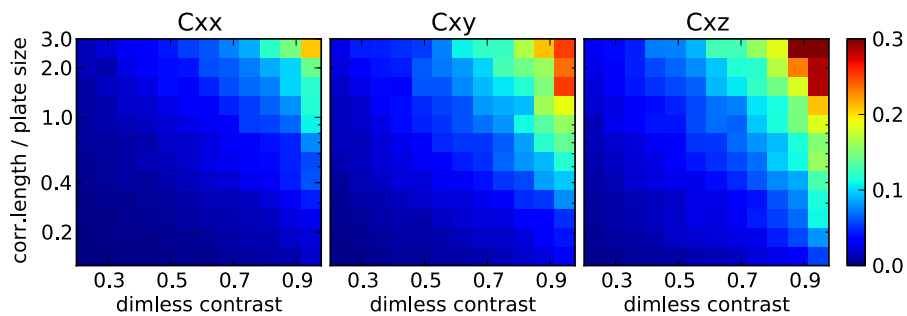

Fig. 3 Results of the statistical analysis in the reduced parameter space: estimates of the standard deviation of the distribution of coupling constants. The coupling constants for shear strain can be derived on this basis analytically (see text)

normal strains with same magnitude but opposite signs (rotation of the coordinates of 45°). Assuming the coupling constants to be normally and independently distributed, the sum is hence again normally distributed with the variance being the sum of the two variances (standard deviation squared).

For rotation around z-axes, this results in a factor of $\sqrt{2}$ in the standard deviation of the coupling constants of shear strain. For the horizontal components, the sum of the squares is dominated by the larger constant for perpendicular axes of rotation and strain, and it is hence on the same order of magnitude.

In general, the coupling constants are the largest for rotation around Z and for perpendicular axes of strain and tilt. Furthermore, they are the larger, the larger the correlation length and the contrast of the elastic constants (under the assumptions stated above and within the parameter space studied). Also it is an important result that SRC due to inhomogeneity is likely to be negligible for short correlation lengths or small contrasts, hence for many applications. Large contrasts can, for example, be expected at volcanoes or young fluvial sediments, where values of up to 0.7 to 0.98 (e.g., volcanic Breccia or Tuff in combination with unconsolidated Ash) can be reached.

2.4 Simulating coupling constants for 3D topography

With the same numerical approach as above, strain rotation coupling due to 3D topography can be estimated. The example presented here consists of the topography around the G ring laser in Wettzell (Germany), a large observatory installation originally intended for geodetical use only that has also been used for rotational seismology in the past years (Schreiber et al. 2006; Igel et al. 2007; Suryanto et al. 2006; Kurrle et al. 2010; Nader et al. 2012).

The model consists of a homogeneous $5 \times 5 \times 3.1$-km^3 cuboid with the topography of Wettzell area on top (25 m resolution, DGM-D model of the German Federal Agency for Cartography and Geodesy). The tetrahedral mesh has a resolution of 15 m at the surface and 200 m in the bulk, the Young's modulus is $E = 68.8$ GPa, and the Poisson ratio is $\nu = 0.28$. The boundary conditions are set to a free surface on the top; the other surfaces are free to move in parallel and are fixed in normal direction. Strain (normal and shear) is imposed as Dirichlet boundary condition, and the coupling constants for each element are computed. The numerical accuracy of the single element values was estimated to be better than 0.05 on the basis of a simulation with 2.5D topography but same mesh parameters, where four of the coupling constants are expected to be zero.

Figure 4 shows all nine coupling constants (three strains times three rotation axis) projected onto the topography model as color scale. The G ring laser location in the center is marked with the green cones. As the ring laser is sensitive to rotation around the z-axes, the last row is the most relevant.

The results show that for the horizontal components of rotations, the coupling is the strongest for perpendicular axes of rotation and strain. It is on the order of 0.4 for large areas and reaches local maxima above 1.0 in the southwest corner, where topography is the roughest. For the vertical component, values are generally smaller and largest for shear strain (which is not surprising because shear strain is equivalent to simultaneous normal strain on two perpendicular axes, see above).

The ring laser site happens to be right in local minima of absolute values for all three constants of rotation around the z-axis. Numerical values averaged over all elements within 100 m radius around the ring laser site (356 elements) are $c_{xz} = -0.016 \pm 0.012$, $c_{yz} = 0.021 \pm 0.010$, and $c_{sz} = 0.02 \pm 0.04$, where the error estimates are the standard deviations of the values within the same radius. It appears by coincidence that topography does not cause large strain rotation coupling at the site, but inhomogeneity on a smaller scale or geometry of the monument and vault (not included in the model) could still cause the same effect. This can only be revealed by the real G ring laser data.

2.5 Estimating coupling constants for the G ring laser in Wettzell, Germany

The instrument setup used by Suryanto et al. (2006) (collocated seismic array and rotational

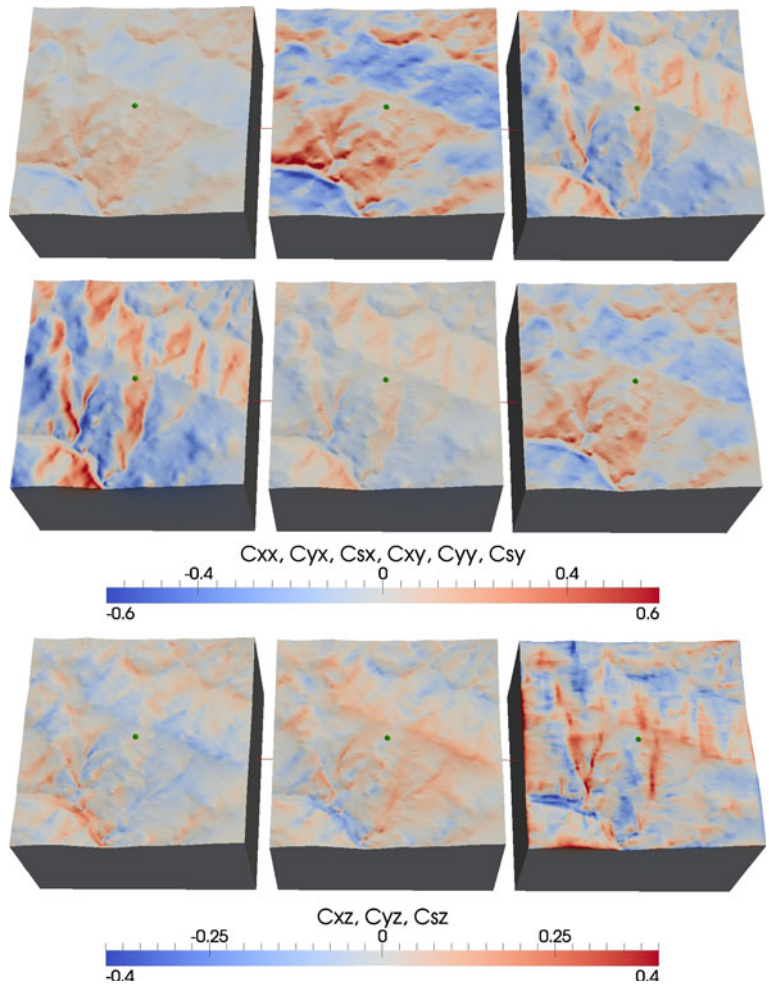

Fig. 4 Wettzell area, 5 × 5 km: Strain rotation coupling constants c_{ij} as defined in Eq. 1 for normal strain in x (east–west, *left*), y (north–south, *center*) and horizontal shear strain (*right*) coupling into rotation around x-, y-, and z-axis (*top* to *bottom*) simulated for a homogeneous medium with topography (25 m resolution, DGM-D model of the German Federal Agency for Cartography and Geodesy), ring laser site is marked with *green cones*. *Upper colorbar* for the upper six models, *lower colorbar* for the lower three

sensor) allows to estimate the coupling constants with a method similar to the one described and used on earth tide tilt data by Lambotte et al. (2006). Assuming that the point rotation measured by the ring laser ω_Z^{RL} equals the rotation averaged over the array area ω_Z^A plus the strain rotation coupling:

$$\omega_Z^{\mathrm{RL}} = \omega_Z^A + \epsilon_N^A c_{NZ} + \epsilon_S^A c_{SZ} + \epsilon_E^A c_{EZ}. \tag{3}$$

The coupling constants can then be estimated by solving the overdetermined linear problem in a least squares sense:

$$\mathbf{d} = \mathbf{G}\mathbf{m} \quad \Rightarrow \quad \mathbf{m} \approx \left(\mathbf{G}^{\mathbf{T}}\mathbf{G}\right)^{-1}\mathbf{G}^{\mathbf{T}}\mathbf{d}, \tag{4}$$

where $d_i = \omega_Z^{\mathrm{RL}}(t_i) - \omega_Z^A(t_i)$, $G_{ij} = \epsilon_j^A(t_i)$ and $\mathbf{m} = (c_{EZ}, c_{SZ}, c_{NZ})^T$. For earthquake data, it is important to use the residual of array derived and point rotation and not the point rotation itself because the rotation around Z-axes is highly correlated with the shear strain for the Love waves, which causes non-unique solutions for the coupling constants otherwise.

The method by Spudich and Fletcher (2009) estimates rotation and strain as well as their covariance matrix from the array data. The variance of the array and the ring laser data is estimated as the variance of the signals 100 s before P-wave arrival. As not only **d** but also **G** is based on measurements and not exactly known, the bootstrapping approach is used to estimate the

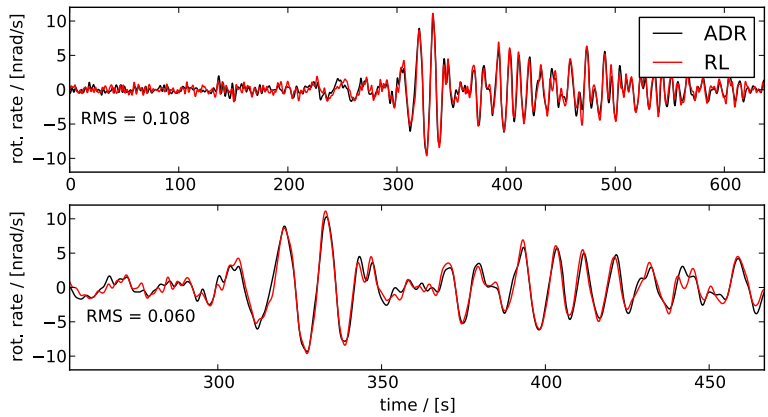

Fig. 5 Rotational seismograms for the February 24th, 2006, M 6.3 Al Hoceima, Morocco event: ring laser (RL) compared to array derived rotation (ADR), bandpass filtered 0.03–0.3 Hz. *Lower trace* is a zoom on the maximum amplitudes

errors of the inversion result **m**: The inversion is performed 10,000 times where each time random noise according to the covariance matrix from the array measurement plus the variance of the ring laser is added to **d** and **G**. The distribution of the results **m** then gives an estimate for the errors of the inversion.

Applying this method to the seismic data in Fig. 5 (time window of the upper trace) yields relatively small values: $c_{EZ} = -0.011 \pm 0.015$, $c_{NZ} = 0.023 \pm 0.027$, and $c_{SZ} = 0.037 \pm 0.031$. This is in agreement with the simulations above in the sense that the values coincide within their errors and the estimates are all small compared to what would be expected on average for the given topography. This also manifests itself in the high correlation (xcorr = 0.96) and low RMS difference (6% in the time window of the lower trace in Fig. 5) between the two measurement methods.

3 Strain rotation coupling effect on rotational seismograms

Whether or not strain-induced rotation is a large effect on rotational seismograms depends not only on the coupling constants but also on the relative magnitude of strain and rotation (radiation pattern, source receiver distance, seismic phases). This will be illustrated in the examples below.

3.1 Near-field of active volcanoes

Recently, Maeda et al. (2011) proposed a method to include tilt in the Green's functions in the moment tensor inversion at volcanoes. Besides the numerical problems they mention, the question arises, whether precise forward simulations of tilt are possible in volcanic environments, where inhomogeneities and rough topography are often present and thus strain-induced rotation can be a significant contribution to the rotational seismograms.

The first example deals with synthetic rotational seismograms simulated for a homogeneous velocity model ($v_p = 3$ km/s, $v_s = 1.5$ km/s, $\rho = 2{,}200$ kg/m^3) including topography of Mt. Merapi volcano (Java, Indonesia), see Fig. 6 (DEM by Gerstenecker et al. 1999, with 45 m resolution, smoothed with a 225-m kernel), and the stations are a subset of a deployed seismic network (Wassermann and Ohrnberger 2001).

The computational domain consists of a cuboid of $10 \times 10 \times 3$ km^3 with the Merapi topography on top (free surface at the top and absorbing boundaries at the other surfaces). The model was meshed with hexahedrons of edge length 300 m in the volume and refined to 100 m at the surface for better topography approximation. The spectral element method (SPECFEM3D, see Peter et al. (2011) and the references therein) is used to generate the seismograms. The source time function consists of a Ricker wavelet with width 1 s and amplitude 1.27×10^{12} Nm ($M_w = 2.0$); source

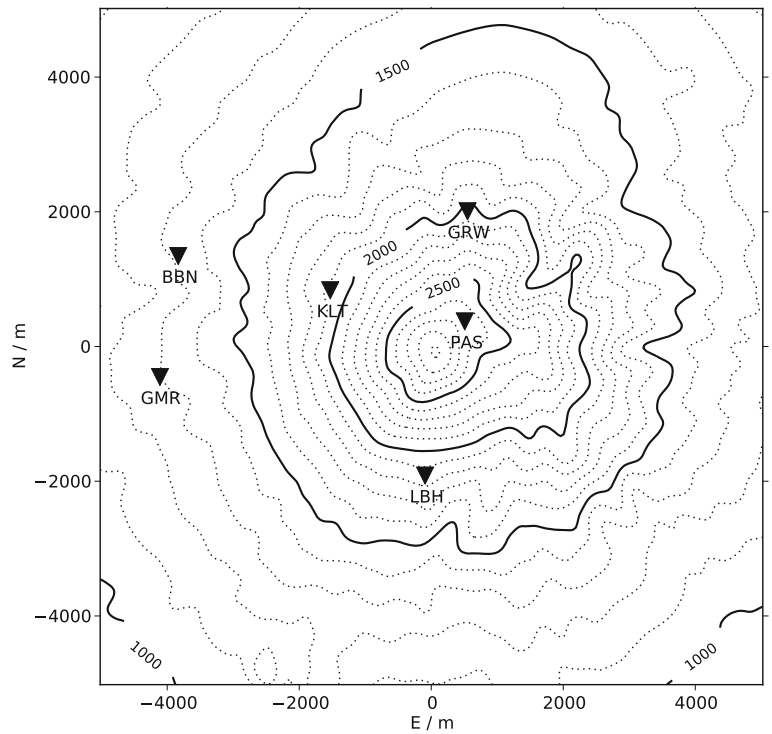

Fig. 6 Mt. Merapi topography model and station locations. DEM with 45 m resolution by Gerstenecker et al. (1999), smoothed with a 225-m kernel

mechanism is an isotropic point source located at 2,000 m height under the summit (2,970 m).

The gradient of the wave field is estimated using a 3D six point stencil of stations, each station in 1 m distance of the translational station in direction of the coordinate axes. Strain and rotation are then computed as the symmetric and antisymmetric part of the gradient.

As topography is included in the model, the possible causes of strain rotation coupling are inhomogeneities and small-scale topography that is not resolved by the mesh (mesh spacing at the surface is 100 m and the topography model had to be significantly smoothed for hexahedral meshing). Figure 7 shows the normalized synthetic rotational seismograms, pure rotation as output of the simulation (black), and with additional strain induced rotation (gray) for 50 realizations of random coupling constants.

Based on the previous considerations, all nine coupling constants (see Section 2.1) are assumed to be normally distributed. The standard deviations are chosen $\sigma_\perp = \sigma_Z = \sigma_S = 0.2$ (for normal strain coupling into rotation perpendicular to the strain, for all strains coupling into rotation around the z-axis, and for shear strain coupling into all three components of rotation, respectively) and $\sigma_\parallel = 0.1$ (for parallel normal strain and rotation axes).

The effect is larger than 50% average RMS (i.e., mean of RMS of the single traces) on the Z component of all stations and up to 314% on the Z-component of GMR. On the horizontal components, the effect is smaller, about 10–20% for most stations, but still reaches the extreme value of 97% for the X-component of LBH. In general, the magnitude of the effect at each station also depends on the radiation patterns, which can be different for rotations and strains (not in this example, due to the isotropic source).

3.2 Far-Field

The second example deals with synthetic rotational seismograms recorded in Wettzell, Germany, for the M6.3 Al Hoceima, Morocco, earthquake (great circle distance 18.5° or 2,058 km). The seismograms were calculated with SPECFEM3D_GLOBE (Komatitsch and

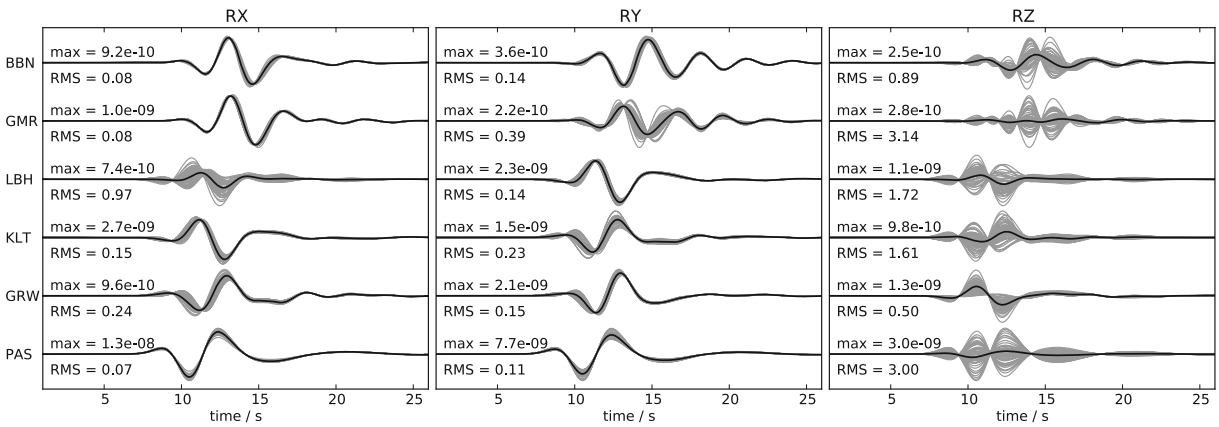

Fig. 7 Normalized synthetic rotational seismograms for an isotropic point source at Mt. Merapi volcano, Indonesia. Clean signal (*black*) and 50 random realizations of strain rotation coupling effect on the rotational seismograms (*gray*); numbers at each traces are maximum amplitudes in radians and RMS errors averaged over the 50 traces; (X, Y, Z) corresponds to (south, east, up)

Tromp 2002a, b) down to 10 s period using the tomographic mantle model S20RTS and crustal model CRUST2.0 and including the effects of attenuation (1D), topography, ocean loading, ellipticity, earth rotation, and self-gravitation. Rotations and strains are calculated using the array with stations WET and S1–S4 as in Suryanto et al. (2006).

Figure 8 shows the clean seismograms and 50 traces with additional strain-induced rotations. The coupling constants are normally distributed with standard deviation $\sigma_{\parallel} = 0.1$ and $\sigma_{\perp} = 0.3$ for

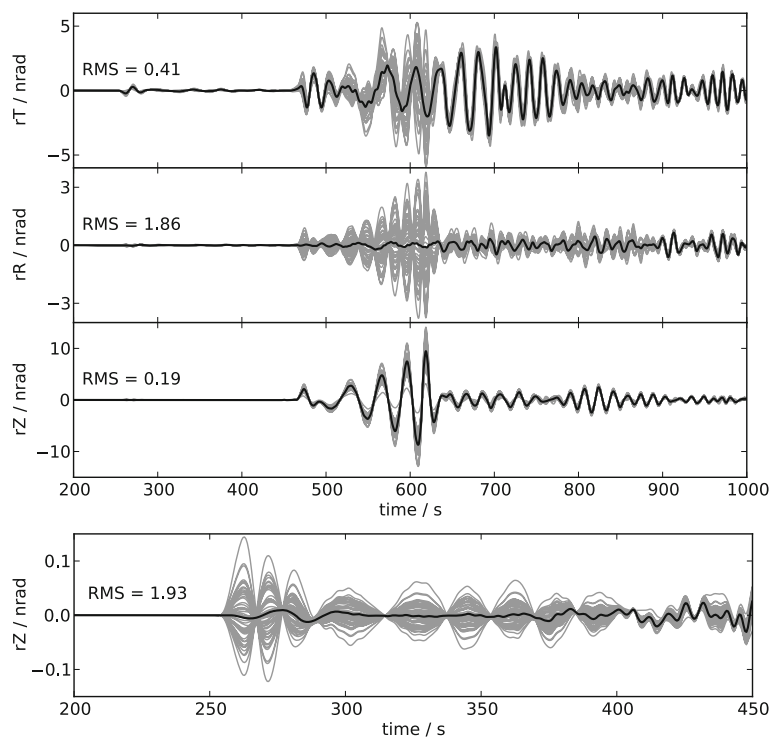

Fig. 8 Synthetic rotational seismograms for the *M*6.3 Al Hoceima, Morocco, earthquake, clean (*black*), and with 50 realizations of random coupling constants, low-pass-filtered at 20 s. TRZ denotes transverse, radial, and up component; RMS denotes the root mean square error averaged over the 50 seismograms in the time window shown. *Lowest trace* zoom into the P-coda of the rZ-component

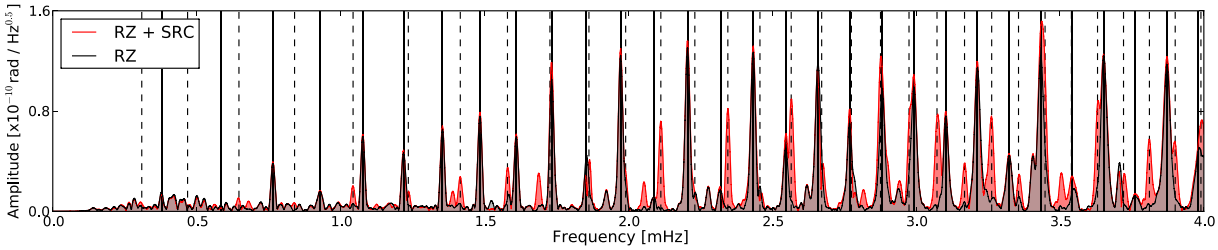

Fig. 9 Amplitude spectrum for rotation around z-axis for 36 h of synthetic data for the M9.0 Tohoku, Japan, earthquake recorded in Wettzell, Germany. Pure rotation with main peaks at toroidal modes (*vertical lines* mark 0Ti modes); strain rotation coupling (here constants are chosen $c_{NZ} = c_{EZ} = -c_{SZ} = 0.2$) can cause additional peaks at spheroidal modes (*dashed lines* mark 0Si modes)

the horizontal component, $\sigma_Z = 0.2$ for the normal strains into vertical component, and $\sigma_S = 0.3$ for all three rotational components.

The largest effects can be seen where the strains are relatively large compared to the rotations: SRC causes large errors in the rR-component (rotation around horizontal axis pointing in direction of the source), which has generally the smallest amplitudes because it is neither sensitive to SH nor to SV waves. Also, rotational signals in the P-coda of the Z-component show up (this is not a contradiction to Pham et al. 2009, who explain the observed P-coda rotations with P to S scattering. SRC can neither explain the correlation between transverse acceleration and rotation rate around Z-axis nor the flat distribution of backazimuths shown in Figs. 4 and 8 in their paper).

Due to the large signals, the Z-component is least affected in S and surface wave trains (which are not well separated yet in the angular distance of 18.5°) but still has an average RMS of 19%.

3.3 Normal mode spectrum

Another effect of strain rotation coupling can be seen in the low-frequency spectrum of rotation around the Z-axes: Fig. 9 shows the amplitude spectrum of 36 h of synthetic seismograms generated with the MINEOS normal mode summation code (Masters et al. 2007) for the CMT solution of the M9.1 Tohoku, Japan earthquake recorded in Wettzell, Germany. Input model is the spherical symmetric non-rotating earth (PREM). The seismograms where recorded at four stations arranged as a cross with diameter of 15 km, which allows computation of rotation and stresses (details on the simulations, see Nader et al. 2012).

In the unperturbed rotation (RZ), the higher peaks all correspond to toroidal eigenmodes. Choosing the SRC constants to be $c_{NZ} = c_{EZ} = -c_{SZ} = 0.2$ (which is moderate in absolute value, but the strains are highly correlated and the signs are chosen such that they add up constructively to show how large the effect could potentially be) and adding the strain-induced rotation, the synthetic spectrum (red in Fig. 9) shows that SRC can cause additional peaks at frequencies corresponding to spheroidal modes that are not expected in the unperturbed rotations: The strains caused by Rayleigh waves that correspond to the spheroidal modes are coupled into the rotation. This effect might be relevant to understand the coupling between spheroidal and toroidal modes observed by Nader et al. (2012).

4 Conclusions

The results show that for tilt correction of horizontal seismograms, point measurements of rotations are necessary if SRC cannot be excluded. Array derived rotation, as a measure of areal rotation and strain, is not able to solve the problem because seismometer arrays then do not necessarily measure the rotation of the individual seismometers themselves. This also implies that forward simulations of rotational motions that generally do not include SRC can differ substantially from

the actual measurements in regimes of large strain rotation coupling. The effect of SRC onto the moment tensor inversion scheme proposed by Maeda et al. (2011) (i.e., including tilt into the moment tensor inversion using simulated Green's functions for rotations) should be carefully tested.

Studies that are mainly focusing on the rotational component of the wave field (in contrast to rotations of single stations) need to carefully select the sites to exclude SRC or correct for it.

Acknowledgements This study was supported by the QUEST Initial Training Network (Marie Curie Actions, www.quest-itn.org) and DFG project Ig16-8. BSAS was supported by a Marie Curie Intra European Fellowship within the 7th European Community Framework Programme (FP7/2007-2013) under grant agreement nr. 235861. We thank the Leibniz Supercomputing Centre for access to computing resources. The manuscript benefited from the constructive comments of two anonymous reviewers.

References

Berger J, Beaumont C (1976) An analysis of tidal strain observations from the united states of america II. The inhomogeneous tide. Bull Seismol Soc Amer 66(6): 1821

Bernauer F, Wassermann J, Igel H (2012) Rotational sensors—a comparison of different sensor types. J Seismol. doi:10.1007/s10950-012-9286-7

Beyreuther M, Barsch R, Krischer L, Megies T, Behr Y, Wassermann J (2010) ObsPy: a python toolbox for seismology. Seismol Res Lett 81(3):530–533. doi:10.1785/gssrl.81.3.530

Cochard A, Igel H, Schuberth B, Suryanto W, Velikoseltsev A, Schreiber U, Wassermann J, Scherbaum F, Vollmer D (2006) Rotational motions in seismology: theory, observation, simulation. In: Teisseyre R, Takeo M, Majewski E (eds) Earthquake source asymmetry, structural media and rotation effects. Springer, New York, pp 391–411

Dunn RW, Mahdi HH, Al-Shukri HJ (2009) Design of a relatively inexpensive ring laser seismic detector. Bull Seismol Soc Amer 99(2B):1437–1442. doi:10.1785/0120080092

Evans JR, Hutt CR, Nigbor RN, de la Torre T (2010) Performance of the new R2 Sensor—presentation at the 2nd IWGoRS meeting in Prague

Gerstenecker C, Läufer G, Snitil B, Wrobel B (1999) Digital elevation models for Merapi. DGG Special Issue

Gomberg J, Agnew D (1996) The accuracy of seismic estimates of dynamic strains: an evaluation using strainmeter and seismometer data from Pifion Flat Observatory, California. Bull Seismol Soc Amer 86(1):212–220

Graizer V (2009) Tutorial on measuring rotations using multipendulum systems. Bull Seismol Soc Amer 99(2B):1064–1072. doi:10.1785/0120080145

Graizer V (2010) Strong motion recordings and residual displacements: what are we actually recording in strong motion seismology? Seismol Res Lett 81(4):635–639. do10.1785/gssrl.81.4.635

Gross L, Bourgouin L, Hale A, Muhlhaus H (2007a) Interface modeling in incompressible media using level sets in Escript. Phys Earth Planet In 163(1-4):23–34. doi:10.1016/j.pepi.2007.04.004

Gross L, Cumming B, Steube K, Weatherley D (2007b) A Python module for PDE-based numerical modelling example: seismic wave propagation. In: Applied parallel computing. State of the Art in Scientific Computing, Springer, New York, pp 270–279. doi:10.1007/978-3-540-75755-9_33

Harrison JC (1976) Cavity and topographic effects in tilt and strain measurement. J Geophys Res 81(2):319–328

Igel H, Cochard A, Wassermann J, Flaws A, Schreiber U, Velikoseltsev A, Pham ND (2007) Broad-band observations of earthquake-induced rotational ground motions. Geophys J Int 168(1):182–196. doi:10.1111/j.1365-246X.2006.03146.x

Kohl ML, Levine J (1995) Measurement and interpretation of tidal tilts in a small array. J Geophys Res 100(B3):3929–3941. doi:10.1007/s11605-011-1421-1

Komatitsch D, Tromp J (2002a) Spectral-element simulations of global seismic wave propagation-I. Validation. Geophys J Int 149(2):390–412. doi:10.1046/j.1365-246X.2002.01653.x

Komatitsch D, Tromp J (2002b) Spectral-element simulations of global seismic wave propagation-II. Three-dimensional models, oceans, rotation and self-gravitation. Geophys J Int 150(1):303–318. doi:10.1046/j.1365-246X.2002.01716.x

Kurrle D, Igel H, Ferreira AMG, Wassermann J, Schreiber U (2010) Can we estimate local Love wave dispersion properties from collocated amplitude measurements of translations and rotations? Geophys Res Lett 37(4):1–5. doi:10.1029/2009GL042215

Lambotte S, Rivera L, Hinderer J (2006) Vertical and horizontal seismometric observations of tides. J Geodyn 41(1–3):39–58. doi:10.1016/j.jog.2005.08.021

Langston CA (2007a) Spatial gradient analysis for linear seismic arrays. Bull Seismol Soc Amer 97(1B):265–280. doi:10.1785/0120060100

Langston CA (2007b) Wave gradiometry in the time domain. Bull Seismol Soc Amer 97(3):926–933. doi:10.1785/0120060152

Langston CA (2007c) Wave gradiometry in two dimensions. Bull Seismol Soc Amer 97(2):401–416. doi:10.1785/0120060138

Lin CJ, Huang HP, Liu CC, Chiu HC (2010) Application of rotational sensors to correcting rotation-induced effects on accelerometers. Bull Seismol Soc Amer 100(2):585–597. doi:10.1785/0120090123

Maeda Y, Takeo M, Ohminato T (2011) A waveform inversion including tilt: method and simple tests. Geophys J Int 184(2):907–918. doi:10.1111/j.1365-246X.2010.04892.x

Masters G, Barmine M, Kientz S (2007) Mineos: user manual. Calif Inst Techbol, Pasadena

Megies T, Beyreuther M, Barsch R, Krischer L, Wassermann J (2011) ObsPy—what can it do for data centers and observatories? Ann Geophys 54(1). doi:10.4401/ag-4838

Mogi K (1958) Relations between the eruptions of various volcanoes and the deformations of the ground surface around them. Bull Earth Res Inst 36:99–134

Nader MF, Igel H, Ferreira AMG, Kurrle D, Wassermann J, Schreiber KU (2012) Toroidal free oscillations of the Earth observed by a ring laser system: a comparative study. J Seismol, this issue

Nigbor RL (1994) Six-degree-of-freedom ground-motion measurement. Bull Seismol Soc Amer 84(5):1665–1669

Nigbor RL, Evans JR, Hutt CR (2009) Laboratory and field testing of commercial rotational seismometers. Bull Seismol Soc Amer 99(2B):1215–1227. doi:10.1785/0120080247

Nolet G (2008) A breviary of seismic tomography: imaging the interior of the earth and sun. Cambridge University Press, Cambridge

Peter D, Komatitsch D, Luo Y, Martin R, Le Goff N, Casarotti E, Le Loher P, Magnoni F, Liu Q, Blitz C, Nissen-Meyer T, Basini P, Tromp J (2011) Forward and adjoint simulations of seismic wave propagation on fully unstructured hexahedral meshes. Geophys J Int 186(2):721–739. doi:10.1111/j.1365-246X.2011.05044.x

Pham ND, Igel H, Wassermann J, Käser M, de la Puente J, Schreiber U (2009) Observations and modeling of rotational signals in the P coda: constraints on crustal scattering. Bull Seismol Soc Amer 99(2B):1315–1332. doi:10.1785/0120080101

Schreiber U, Hautmann JN, Velikoseltsev A, Wassermann J, Igel H, Otero J, Vernon F, Wells JPR (2009) Ring laser measurements of ground rotations for seismology. Bull Seismol Soc Amer 99(2B):1190–1198. doi:10.1785/0120080171

Schreiber U, Velikoseltsev A, Igel H, Cochard A, Flaws A, Drewitz W, Müller F (2003) The GEOsensor: a new instrument for seismology. GEO-TECHNOLOGIEN Science Report 3, pp 12–13

Schreiber U, Stedman GE, Igel H, Flaws A (2006) Ring laser gyroscopes as rotation sensors for seismic wave studies. In: Teisseyre R, Takeo M, Majewski E (eds) Earthquake source asymmetry, structural media and rotation effects. Springer, New York

Spudich P, Fletcher JB (2008) Observation and prediction of dynamic ground strains, tilts, and torsions caused by the Mw 6.0 2004 Parkfield, California, earthquake and aftershocks, derived from UPSAR Array observations. Bull Seismol Soc Amer 98(4):1898–1914. doi:10.1785/0120070157

Spudich P, Fletcher JB (2009) Software for inference of dynamic ground strains and rotations and their errors from short baseline array observations of ground motions. Bull Seismol Soc Amer 99(2B):1480–1482. doi:10.1785/0120080230

Spudich P, Steck LK, Hellweg M, Fletcher JB, Baker LM (1995) Transient stresses at Parkfield, California, produced by the M 7.4 Landers earthquake of June 28, 1992: observations from the UPSAR dense seismograph array. J Geophys Res 100:675–675

Suryanto W, Igel H, Wassermann J, Cochard A, Schuberth B, Vollmer D, Scherbaum F, Schreiber U, Velikoseltsev A (2006) First comparison of array-derived rotational ground motions with direct ring laser measurements. Bull Seismol Soc Amer 96(6):2059–2071. doi:10.1785/0120060004

Wassermann J, Ohrnberger M (2001) Automatic hypocenter determination of volcano induced seismic transients based on wavefield coherence—an application to the 1998 eruption of Mt. Merapi, Indonesia. J Volcanol Geoth Res 110(1–2):57–77. doi:10.1016/S0377-0273(01)00200-1

Wassermann J, Lehndorfer S, Igel H, Schreiber U (2009) Performance test of a commercial rotational motions sensor.Bull Seismol Soc Amer 99(2B):1449–1456. doi:10.1785/0120080157

Wielandt E, Forbriger T (1999) Near-field seismic displacement and tilt associated with the explosive activity of Stromboli. Ann Geofisc 42(3):407–416

Yoon M (2005) Deep seismic imaging in the presence of a heterogeneous overburden—numerical modelling and case studies from the Central Andes and Southern Andes. Ph.D., Freie Universität Berlin. doi:10.1016/0926-9851(93)90007-L